JGR Space Physics

METHOD
10.1029/2023JA031757

Key Points:

- We test the performance of the Wang method II in the Martian magnetosheath using the magnetic field data from the Tianwen-1 orbiter
- The zero offset determined by the Wang method II is close to that calculated by using the potential Alfvénic fluctuation in the solar wind
- The test results show that this method is suitable for determining the zero offset of the Tianwen-1 orbiter in the Martian magnetosheath

Correspondence to:
Y. M. Wang and T. L. Zhang,
ymwang@ustc.edu.cn;
Tielong.Zhang@oeaw.ac.at

Citation:
Wang, G. Q., Xiao, S. D., Wu, M. Y., Zhao, Y. D., Jiang, S., Pan, Z. H., et al. (2024). Calibration of the zero offset of the fluxgate magnetometer on board the Tianwen-1 orbiter in the Martian magnetosheath. *Journal of Geophysical Research: Space Physics*, *129*, e2023JA031757. https://doi.org/10.1029/2023JA031757

Received 7 JUN 2023
Accepted 19 DEC 2023

Calibration of the Zero Offset of the Fluxgate Magnetometer on Board the Tianwen-1 Orbiter in the Martian Magnetosheath

Guoqiang Wang[1,2], Sudong Xiao[1,2], Mingyu Wu[1,2], Yangdong Zhao[3], Song Jiang[3], Zonghao Pan[4,5], Xinjun Hao[4,5], Yiren Li[4,5], Kai Liu[4,5], Yutian Chi[6], Zhuxuan Zou[4,5], Manming Chen[4,5], Zhenpeng Su[4,5], Chenglong Shen[4,5], Jingnan Guo[4,5], Long Cheng[4,5], Zhiyong Wu[4,5], Mengjiao Xu[6], Yuming Wang[4,5], and Tielong Zhang[1,2,5,7]

[1]Institute of Space Science and Applied Technology, Harbin Institute of Technology, Shenzhen, China, [2]Shenzhen Key Laboratory of Numerical Prediction for Space Storm, Harbin Institute of Technology, Shenzhen, China, [3]Aerospace System Engineering, Shanghai, China, [4]Deep Space Exploration Laboratory/School of Earth and Space Sciences, University of Science and Technology of China, Hefei, China, [5]CAS Center for Excellence in Comparative Planetology/CAS Key Laboratory of Geospace Environment/Mengcheng National Geophysical Observatory, University of Science and Technology of China, Hefei, China, [6]Institute of Deep Space Sciences, Deep Space Exploration Laboratory, Hefei, China, [7]Space Research Institute, Austrian Academy of Sciences, Graz, Austria

Abstract High-precision measurements of the magnetic field are critical to explore the near-Mars environment. The Mars Orbiter MAGnetometer (MOMAG) is one of seven payloads on board the Tianwen-1 orbiter. Its zero offset needs regular calibration, and the Wang-Pan method I is applied to the MOMAG when the Tianwen-1 orbiter is in the solar wind. The orbiter will remain out of the solar wind over tens of days each year, a method is necessary to ensure the accuracy of the zero offset during this period. Recently, a new method was proposed by Wang (2022b), https://doi.org/10.3847/1538-4357/ac822c, which is referred to as the Wang method II for ease of description. Here, we test the performance of this method using the MOMAG data measured in the Martian magnetosheath. We find that the zero offset $\mathbf{O}_w$ determined by the Wang method II varies around the zero offset $\mathbf{O}_{wp}$ calculated by the Wang-Pan method I using the potential Alfvénic fluctuations in the solar wind. After smoothing with a temporal window of 27 days, $\mathbf{O}_w$ is able to achieve an accuracy close to $\mathbf{O}_{wp}$. If the data segment has no gaps and its duration is < 27 days, the smoothed $\mathbf{O}_w$ might have an error >2 nT, but the error tends to be smaller if the segment's duration is longer. Our tests suggest that the Wang method II is suitable for the in-flight calibration of the MOMAG when the Tianwen-1 orbiter remains out of the solar wind.

1. Introduction

Tianwen-1, launched on 23 July 2020, is China's first exploration mission to Mars (Li et al., 2021; Zou et al., 2021). Its scientific objectives are to investigate the Martian ionosphere and magnetosphere and their relation with the solar wind, the Martian atmosphere, the Martian surface and sub-surface, the topography and geological structure, subsurface ice, and so on (Li et al., 2021; Zou et al., 2021). To achieve these scientific objectives, there are seven payloads on the orbiter and six payloads on the rover (Li et al., 2021). The orbit inclination of the Tianwen-1 orbiter is 90° ± 5°, and its orbital period is ~7.8 hr (Li et al., 2021). The altitudes of its periareon and apoareon are ~265 and 11,900 km, respectively (Li et al., 2021).

Although Mars has no global magnetic field, a magnetosphere is formed surrounding Mars when it interacts with the solar wind (Bertucci et al., 2011; Dubinin et al., 2019). The Mars' crustal magnetic field can affect its induced magnetosphere boundary (Connerney et al., 2005; Edberg et al., 2009). A plenty of physical phenomena such as instabilities, magnetic reconnections, ion escape and photoionization happen in the Martian magnetosheath, magnetosphere and ionosphere as well as the solar wind (Chai et al., 2019; DiBraccio et al., 2015; Fang et al., 2018; Liu et al., 2021; Wang et al., 2021; Xu et al., 2018). The magnetic field is crucial to investigate the physical phenomena or dynamics in the near-Mars space (Connerney et al., 2015; Liu et al., 2021).

Measurements of the magnetic field are provided by the Mars Orbit MAGnetometer (MOMAG) aboard the Tianwen-1 orbiter (Liu et al., 2020). MOMAG consists of two identical fluxgate magnetometer (FGM) sensors, mounted on a 3.19-m boom with a separation of ~0.9 m (Liu et al., 2020; Wang et al., 2023; Yang et al., 2021;

Table 1
Methods of the In-Flight Calibration of the Spaceborne Magnetometer

Physical phenomenon on which the method is based	Equation-based method	Probability-based method
Alfvén waves	Davis & Smith, 1968 Belcher, 1973 Hedgecock, 1975	Wang & Pan, 2021a
Mirror modes	Plaschke & Narita, 2016 Plaschke et al., 2017	Wang & Pan, 2021b Wang, 2022a
Current sheets		Wang & Pan, 2022
Any magnetic field variations in the solar wind		Wang, 2022b Meng & Wang, 2023

Zhou et al., 2019). Both sensors sample the magnetic field at an intrinsic frequency of 128 Hz, but will be operated at a frequency of 32 Hz (1 Hz) when the orbiter is near the periareon or apoareon (the rest of the orbit) to meet telemetry allocations (Liu et al., 2020). The magnetic field measured by FGMs on board the spacecraft generally consists of natural magnetic field, field induced by the spacecraft, and the instrumental offset (Pope et al., 2011; Russell et al., 2016). The magnetic field induced by the spacecraft can be divided into dynamic and static fields (Pope et al., 2011), where the dynamic field can be removed by the dual point method (Ness et al., 1971; Pope et al., 2011). Since the static field and instrumental offset are difficult to distinguish, both are regarded as the zero offset (Leinweber et al., 2008). The zero offset slowly varies, thus, it needs regular in-flight calibration.

Alfvén waves (Cheng et al., 2022; Davis & Smith, 1968; Meng et al., 2018; Pan et al., 2019; Wang & Pan, 2021a), mirror mode structures (Hu, Wang, Pan, & Zhang, 2022; Plaschke et al., 2017; Plaschke & Narita, 2016; Wang & Pan, 2021b), and current sheets (Wang & Pan, 2022) can be used to determine the zero offset of the spaceborne FGM. Table 1 lists the papers on the in-flight calibration methods of FGMs, which can be divided into two groups: zero offsets determined by equations (Belcher, 1973; Davis & Smith, 1968; Hedgecock, 1975; Plaschke et al., 2017; Plaschke & Narita, 2016) and probabilities (Meng & Wang, 2023; Wang, 2022a, 2022b; Wang & Pan, 2021a, 2021b, 2022). Since the interplanetary magnetic field (IMF) is highly Alfvénic (see Leinweber et al., 2008), the methods based on Alfvén waves are suitable for the spacecraft in the solar wind. The methods proposed by Wang and Pan (2021a) have a good performance in the solar wind, thus this method is selected to determine the zero offset of the MOMAG when the Tianwen-1 orbiter is in the solar wind (Zou et al., 2023).

When the Tianwen-1 orbiter remains out of the solar wind over tens of days, the zero offsets determined before leaving and after entering the solar wind can be used to perform the in-flight calibration for this long period by interpolation. Two important prerequisites for this operation are as follows: (a) the zero offset has no significant change over this period, and (b) no gaps exist in the magnetic field data. Actually, some gaps with a duration of at least several hours exist in the MOMAG data from 2022 March 1 to 2022 June 30, during which the orbiter remained out of the solar wind. These gaps divided the data into several segments. Generally, the zero offset is expected to have little change in a short period, such as 1 or 2 days. During the processing of removing the orbiter-generated field, one can find the dynamic field with a sudden change as shown in Figure 1 in Pope et al. (2011). Such dynamic fields always occur as pairs with equal and opposite vector components, and only correcting pairs has little effect on the zero offset (Pope et al., 2011). If some dynamic fields do not occur as pairs for a certain segment of the continuous data, an unknown constant is inevitably added into the zero offset. Therefore, the zero offset can be regarded as consisting of instrumental offset, static field and an unknown constant caused by the processing of removing the dynamic field, which means that each segment of the continuous data needs to be calculated separately. Compared to the calibration in the solar wind, a different method needs to perform the calibration for these data segments.

There are many mirror mode structures and current sheets in the planetary magnetosheath (Tsurutani et al., 2011; Volwerk et al., 2008, 2016; Wu et al., 2021), thus the methods based on these structures might be suitable for the spacecraft in the planetary magnetosheath. The method proposed by Wang (2022a) can achieve a high accuracy of the zero offset using hole-like mirror mode structures in the terrestrial magnetosheath. Before calculation the zero offset, the data during each hole-like mirror mode structure are used to perform the minimum variance analysis (MVA; Sonnerup & Scheible, 1998). To perform MVA, a structure is considered to be good if it has enough data points, such as 10. Unfortunately, no enough good hole-like mirror modes or current sheets can be found in the Martian magnetosheath to perform the in-flight calibration for the MOMAG. Wang (2022b) proposed a method of determining the zero offset using any magnetic field data in the solar wind. For a convenient description, we refer to this method as Wang method II, and refer to the method proposed by Wang and Pan (2021a) as

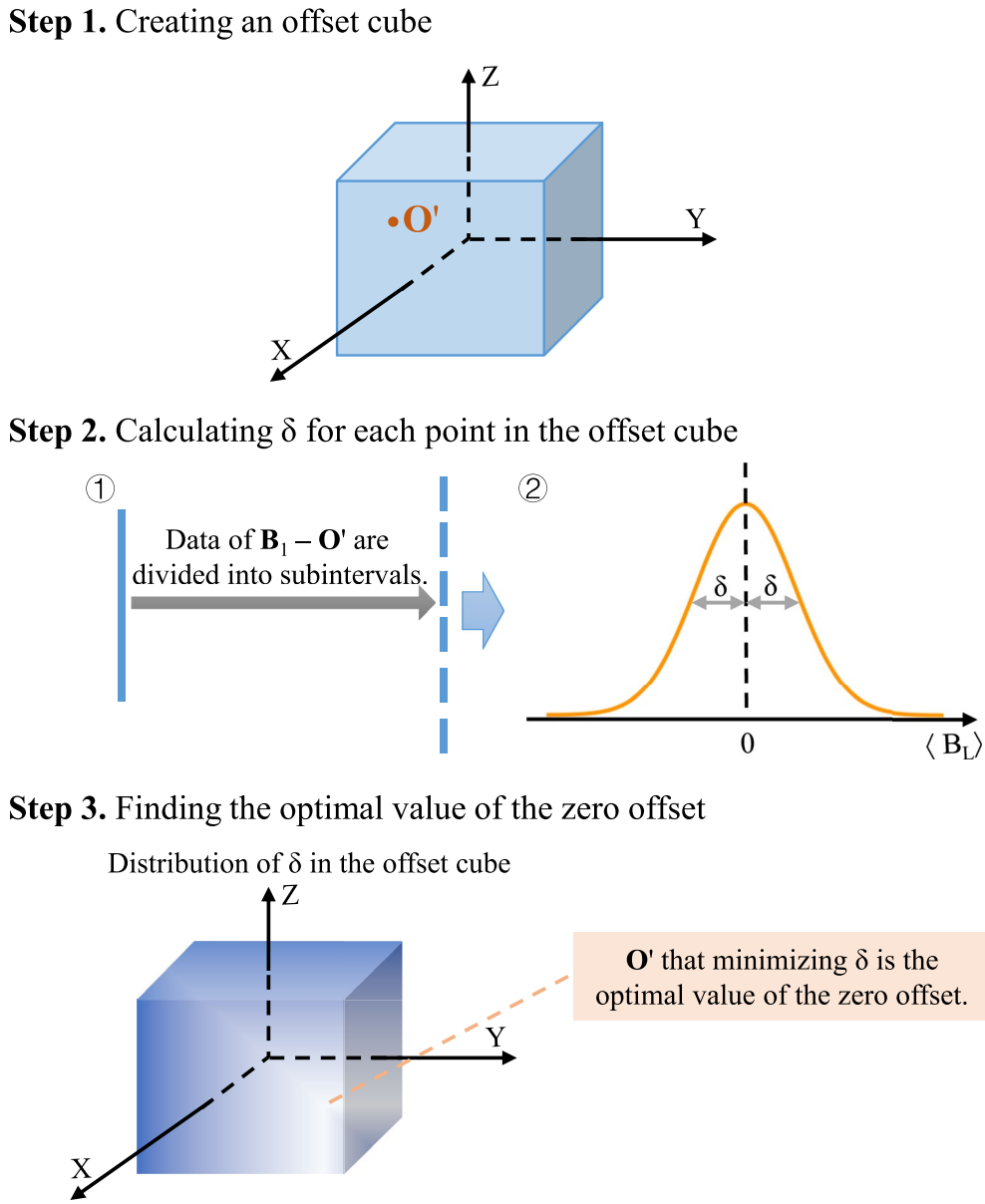

Figure 1. A diagram of the zero offset calculation of the Wang method II. $\mathbf{B}_1$ denotes the uncalibrated magnetic field data. **O'** denotes a certain point in the offset cube. δ denotes the standard deviation of the fitted normal distribution of $\langle B_L \rangle$.

Wang-Pan method I. Wang (2022c) tested the Wang method II in the Martian magnetosheath using the calibrated magnetic field data in the Mars-centered Solar Orbital (MSO) coordinate system from the Mars Atmosphere and Volatile EvolutioN (MAVEN) spacecraft (Jakosky et al., 2015), and found that its calculation error varies with a period of ~27 days and has a 57.3% probability of being less than 2.0 nT. The MSO coordinate system is defined as its *x*-axis points the Sun, *y*-axis points opposite to the Martian orbital angular velocity, and *z*-axis completes the right-handed coordinated system. The magnetic field data used by Wang (2022c) are in the MSO coordinate system and have been calibrated, however, whether the Wang method II is suitable for the MOMAG using the uncalibrated data in the orbiter coordinate system is unknown.

In this study, we test the performance of the Wang method II in the Martian magnetosheath using the uncalibrated MOMAG data in the orbiter coordinate system. We will show that this Method can obtain results similar to the Wang-Pan method I and therefore can be used to determine the zero offset when the Tianwen-1 orbiter remains out of the solar wind over tens of days.

2. Wang Method II

The LMN coordinate system is a local coordinate system, which L, M and N axes denote the maximum, intermediate and minimum variance directions of the magnetic field (Sonnerup & Scheible, 1998). The IMF data **B** can be divided into subintervals with a duration of tens of seconds. For a certain subinterval, the average of the L component of the magnetic field $\langle B_L \rangle$ can be calculated by MVA using the data during this whole subinterval. Wang (2022b) found that the distribution of $\langle B_L \rangle$ approximately obeys a normal distribution if the number of the used subintervals is large enough. Using the data of **B** plus a constant vector in the spacecraft coordinate system, the distribution of $\langle B_L \rangle$ also approximately obeys a normal distribution, but its standard deviation δ would change. Interestingly, δ has a minimum value when the constant vector is ≈ 0, which might be supported by the fact that the median is ∼0 for each component of the IMF over a long enough period (Wang, 2022b). Such a property can be used as an indicator to find out the zero offset of the spaceborne FGM (Wang, 2022b).

Figure 1 shows the diagram of the zero offset calculation of the Wang method II, which has three steps as follows (see Wang, 2022b).

a. Step 1 is to build an offset cube according to the possible range of the IMF strength. Any point in this offset cube has a possibility to be the zero offset.
b. Step 2 is to obtain δ for a certain point **O'** in the offset cube as follows.

1. The uncalibrated data $\mathbf{B}_1$ (= **B** + **O**) is changed to $\mathbf{B}_2 = \mathbf{B}_1 - \mathbf{O'}$ at the point **O'** in the offset cube. Then $\mathbf{B}_2$ is divided into subintervals with a duration of T, where T can be set to be a value in the range of 10–300 s according to the resolution of $\mathbf{B}_2$ as well as the period of the IMF fluctuation. The temporal resolution of $\mathbf{B}_2$ determines the number of data points within the subinterval with a certain duration. In order to perform MVA, we can require that the number of data points in each subinterval is at least 10. There is no limit on the period of the IMF fluctuation. Nevertheless, we can require that at least one component of the magnetic field has a variation of >0.5 nT during the whole subinterval.
2. Next, we calculate $\langle B_L \rangle$ for each subinterval by MVA using $\mathbf{B}_2$, and then obtain the fitted normal distribution of $\langle B_L \rangle$ of N adjacent subintervals, where N is the number of these subintervals. Thus, the standard deviation δ of the fitted normal distribution can be obtained for the point **O'.**
3. Step 3 is to determine the zero offset. We can obtain the values of δ for all the points in the offset cube. The point with the minimum δ is regarded as the optimum zero offset.

In the Martian magnetosheath, Wang (2022c) found that the distribution of $\langle B_L \rangle$ also proximately obeys a normal distribution, which might be associated with the finding that the median of the magnetic field distribution in the Martian magnetosheath is close to 0 over a long period (see Wang, 2022c). Thus, the Wang method II might be work in the Martian magnetosheath.

3. Application to Tianwen-1 Orbiter

3.1. Zero Offset Determined by the Wang Method II

The MOMAG data with a resolution of 1 s from 13 November 2021 to 3 January 2022 are used. In our rest paper, all the vector data are in the orbiter coordinate system unless otherwise stated. This coordinate system is defined as the *X*-axis pointing to the flight direction, the *Z*-axis pointing to the Mars at the periareon, and the *Y*-axis meeting the right-hand system (Li et al., 2021). MOMAG was installed in the *Z*-axis direction (Li et al., 2021).

The measurements of the MOMAG sensors are $\mathbf{B}_{s1} = \mathbf{B}_a + \mathbf{B}_{sc1} + \mathbf{O}_{s1}$ and $\mathbf{B}_{s2} = \mathbf{B}_a + \mathbf{B}_{sc2} + \mathbf{O}_{s2}$, respectively, where $\mathbf{B}_a$ is the natural magnetic field, $\mathbf{B}_{sc1}$ and $\mathbf{B}_{sc2}$ are the dynamic fields measured by the sensor 1 and 2, $\mathbf{O}_{s1}$ and $\mathbf{O}_{s2}$ are the zero offsets of the sensor 1 and 2, respectively. Before performing calculation of the zero offset, the orthogonality and sensitivity calibrations of MOMAG have already been done, and the dynamic field has also been removed by the dual point method (Ness et al., 1971; Pope et al., 2011). After removing the dynamic field, $\mathbf{B}_{s1} - \mathbf{B}_{sc1}$ (or $\mathbf{B}_{s2} - \mathbf{B}_{sc2}$) is equal to $\mathbf{B}_m$ (=$\mathbf{B}_a$ + **O**), where the zero offset **O** is $\mathbf{O}_{s1}$ (or $\mathbf{O}_{s2}$).

The MOMAG data are not continuous from 13 November 2021 to 3 January 2022. Some gaps divide these data into several segments. The data in each segment are continuous, which needs to be calculated separately. For processing convenience, we add different constant vectors to $\mathbf{B}_m$ in different data segments so that the average magnetic field is 0 during each segment. In this step, $\mathbf{B}_m$ has been changed to $\mathbf{B}_{m2}$, which is used to determine the zero offset by the Wang method II.

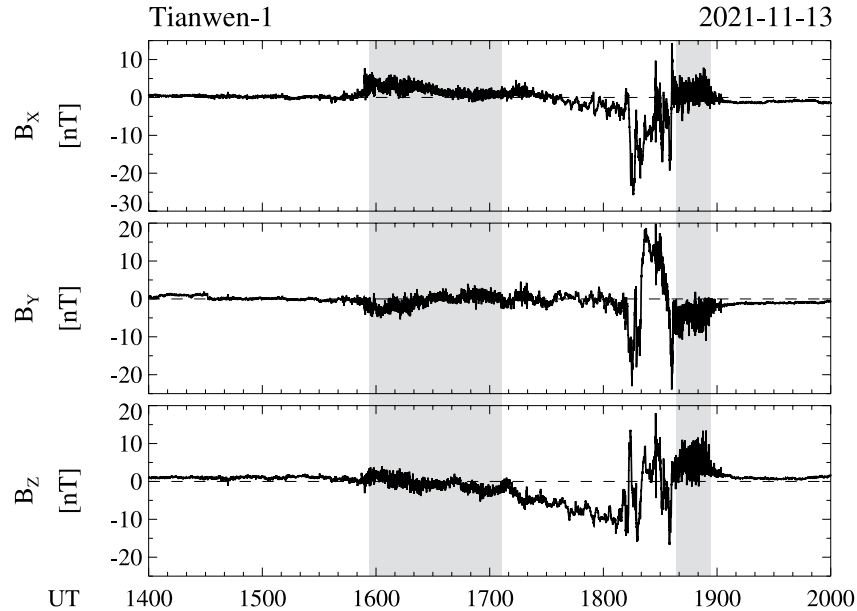

Figure 2. Three components of $\mathbf{B}_{m2}$ in the orbiter coordinate system between 14:00 and 20:00 UT on 13 November 2021. The gray shadows denote the intervals of the magnetosheath selected to perform the in-flight calibration.

Figure 2 shows $\mathbf{B}_{m2}$ between 14:00 and 20:00 UT on 13 November 2021. Compared to the solar wind, the magnetic field in the magnetosheath has strong fluctuations. The Martian magnetic pileup boundary and bow shock are variable with the change of the solar wind (Edberg et al., 2008). To make sure that the selected data are in the magnetosheath or solar wind, we visually select the interval of the Tianwen-1 orbiter in the Martian magnetosheath as well as the solar wind according to the models of the Martian magnetic pileup boundary and bow shock (Edberg et al., 2008), position of the orbiter in MSO coordinate system as well as the intensity of the magnetic field fluctuation. The gray shadows in Figure 2 show two selected intervals in the magnetosheath.

For each data segment, we determine the zero offset using the steps shown in Figure 1 after visually obtaining the intervals of the orbiter in the Martian magnetosheath. The details for each step are given as follows.

a. An offset cube is built according to the possible range of the magnetic field strength in the Martian magnetosheath. The offset cube is divided into bins with a side length of 0.1 nT.
b. Then, we calculate the values of δ for all the points in the offset cube as follows.
    1. For a given interval, the durations of the subintervals are empirically set to 10, 20 and 30 s, respectively. For each value of T, the duration of the *i*th subinterval is set to $0.2 \cdot i \cdot T + [T_0, T_0 + T]$, where T_0 is the start time of this interval.
    2. Using more adjacent subinterval events might have a smaller calculation error of the zero offset (Wang, 2022b). Here, 10,000 or 20,000 adjacent subintervals of $\mathbf{B}_{m2}$ are used to determine the zero offset. The data of all these subintervals are required to be selected in a temporal window of 10 days.
    3. At the point $\mathbf{O}'$, $\mathbf{B}_{m2}$ is changed to $\mathbf{B}_2 = \mathbf{B}_{m2} - \mathbf{O}'$. For each subinterval, $\langle B_L \rangle$ can be determined by MVA using the data of $\mathbf{B}_2$. After obtaining the values of $\langle B_L \rangle$ for all the 10,000 or 20,000 adjacent subintervals, we determine the standard deviation δ of the fitted normal distribution of $\langle B_L \rangle$.
    4. Similarly, the values of δ can be obtained for all the grid points in the offset cube.
c. The point with a minimum δ is selected to be the optimum zero offset of MOMAG. The average time of the used subintervals is selected to be the time of the estimated zero offset.
d. To calculate the next zero offset, the subscripts for the selected 10,000 and 20,000 adjacent subintervals increase by 2,000 and 4,000, respectively.

Figure 3 shows an example of the determination of the zero offset when using the first 10,000 and 20,000 adjacent subinterval events in the data segment between 13:06 UT on 14 November 2021 and 05:31 UT on 22 November 2021. Figures 3a and 3c show the distribution of $\langle B_L \rangle$ determined by using the data of $\mathbf{B}_2$ when $\mathbf{O}' = 0$. The red curves are the fitted normal distributions, which indicate that both distributions approximately obey normal

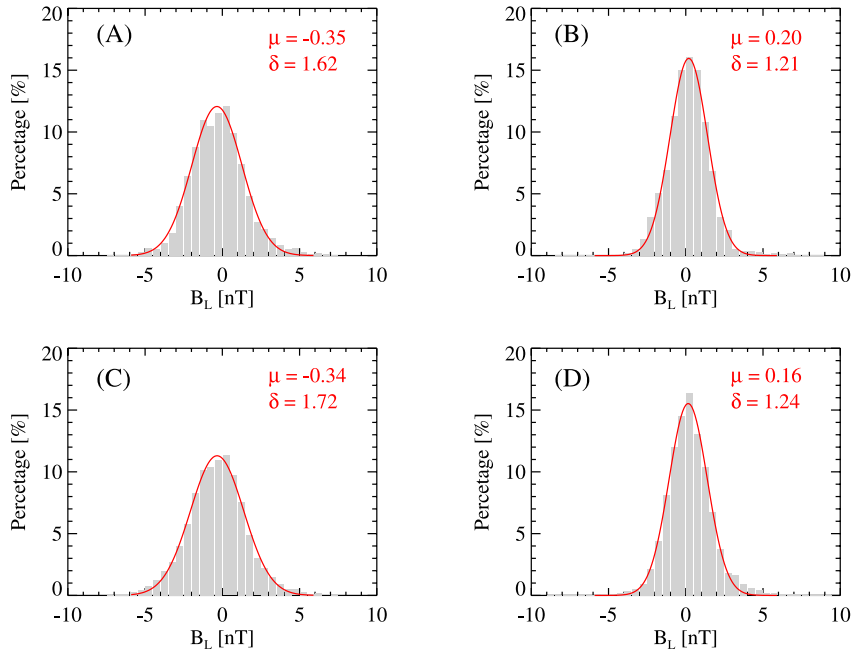

Figure 3. Distributions of $\langle B_L \rangle$ of 10,000 (up) and 20,000 (bottom) adjacent subinterval events determined by using the data of $\mathbf{B}_2$ when **O'** is 0 (left) and the optimum zero offset (right), respectively. The red curves denote the fitted normal distributions, and the mean μ and standard deviation δ are also given.

distributions. Following the above procedure, the zero offsets are determined to be [1.5, −0.6, −2.4] nT and [1.4, −0.1, −2.9] nT when using these 10,000 and 20,000 adjacent subinterval events, respectively. Note that these zero offsets are for the entire data segment from 13:06 UT on 14 November 2021 to 05:31 UT on 22 November 2021. Figures 3b and 3d show the distribution of $\langle B_L \rangle$ determined by using the data of $\mathbf{B}_2$ when **O'** is the above estimated zero offset, and both distributions approximately obey normal distributions with a smaller standard deviation δ compared to those in Figures 3a and 3c. One can find that the distribution of $\langle B_L \rangle$ for the 10,000 adjacent subinterval events is very similar to that for the 20,000 adjacent subinterval events.

3.2. Comparison of the Zero Offsets Determined by Two Methods

To test whether the zero offset determined by the Wang method II is reliable or not, we compare it to the zero offset determined by the Wang-Pan method I. The calculation procedure of the Wang-Pan method I follows the procedure proposed by Hu, Wang, Pan, and Pan (2022). The fluctuation event is considered to be a potential Alfvénic fluctuation event if at least one point in the offset cube has a value of $\delta B_T / \sqrt{\delta B_X^2 + \delta B_Y^2 + \delta B_Z^2} < 0.3$, where δB_X, δB_Y, δB_Z, and δB_T are the standard deviations of B_X, B_Y, B_Z, and B_T, respectively. The threshold 0.3 is an empirical value. If this value is set to be smaller, the selected potential Alfvénic fluctuation events tend to be less. In total, we find 375 potential Alfvénic fluctuation events in the solar wind from 13 November 2021 to 3 January 2022.

Figures 4a and 4b shows a potential Alfvénic fluctuation event between 00:44:42 and 00:45:41 UT on 15 November 2021. The data in Figures 4a and 4b are $\mathbf{B}_{m2} - \mathbf{O'}$, where $\mathbf{O'} = 0$ and $\mathbf{O'} = [-2.28, -0.28, 0.07]$ nT, respectively. During the event, the standard deviations of $|\mathbf{B}_{m2} - \mathbf{O'}|$ are ∼0.86 and 0.06 nT in Figures 4a and 4b, respectively. Although $|\mathbf{B}_{m2} - \mathbf{O'}|$ in Figure 4b is almost constant, each component of $\mathbf{B}_{m2} - \mathbf{O'}$ has a large variation, which meets the expectation of an Alfvénic fluctuation.

We calculate the zero offset using 10 adjacent potential Alfvénic fluctuation events for each data segment. Figure 4c shows an example of the zero offset determination. The dots in each color denote the optimal offset line (OOL) of a certain event, and the straight line in that color denotes the fitted optimal offset line (FOOL) of the corresponding event. The red triangle denotes the zero offset (=[-0.7, 0.3, −0.5] nT) determined by these 10 FOOLs.

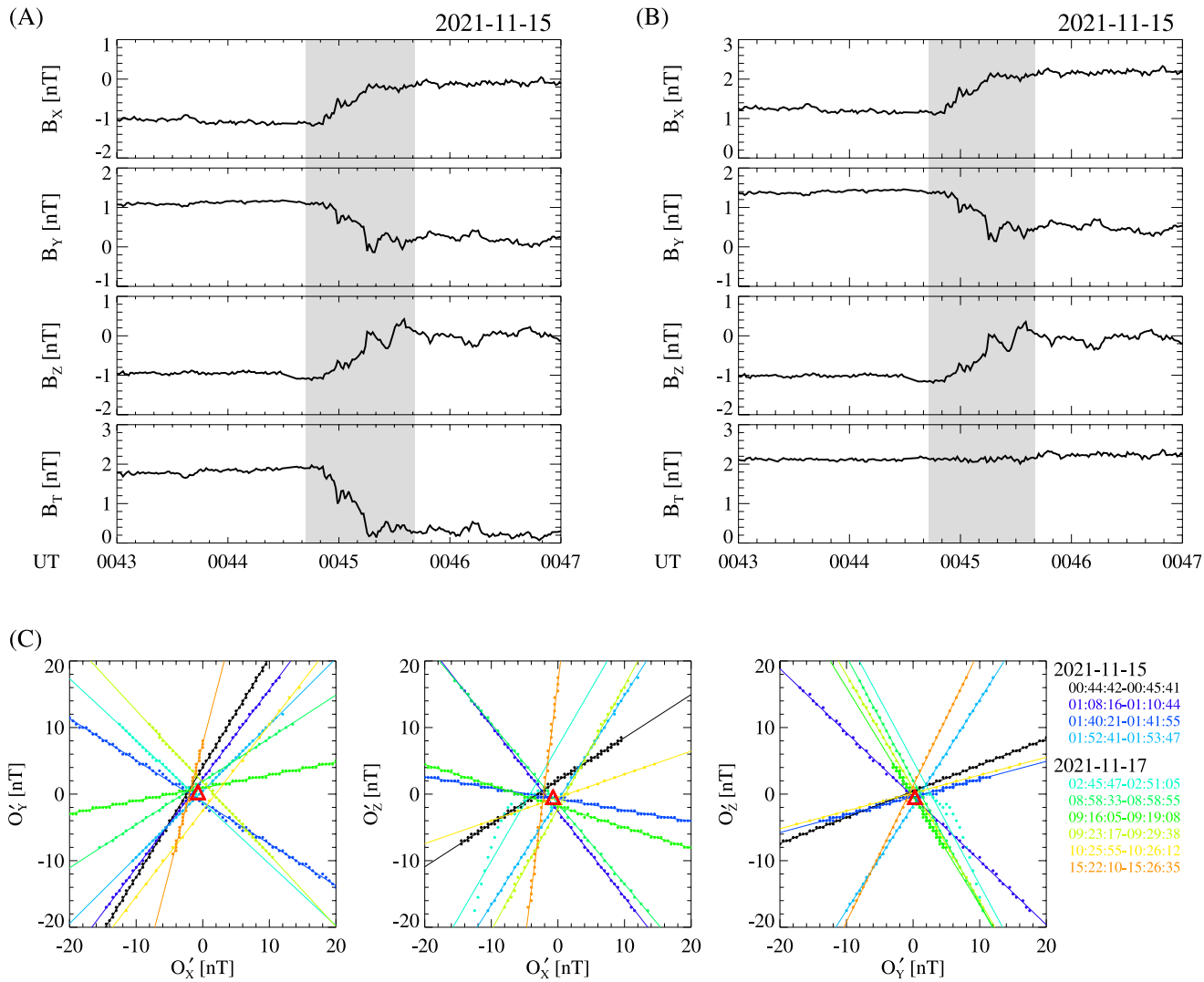

Figure 4. (a) $\mathbf{B}_{m2}$ and its strength between 00:43 and 00:47 UT on 15 November 2021. (b) $\mathbf{B}_{m2}$ - [−2.28, −0.28, 0.07] nT and its strength. (c) An example of the zero offset determined by the Wang-Pan method I using 10 potential Alfvénic fluctuation events. The time intervals of the 10 events are given. The dots with the same color denote the OOL, and the straight line in that color denote the FOOL. The red triangle denotes the result of the zero offset.

The gaps divide the data from 13 November 2021 to 3 January 2022 into five segments as shown in the gray shaded region in Figure 5. Figure 5 also shows the zero offsets $\mathbf{O}_{w1}$ (green) and $\mathbf{O}_{w2}$ (orange) determined by the Wang method II using 10,000 and 20,000 adjacent subinterval events only in the magnetosheath for each data segment, respectively. For comparison, the zero offsets $\mathbf{O}_{WP}$ determined by the Wang-Pan method I using the potential Alfvénic fluctuation events only in the solar wind are also shown. As a whole, $\mathbf{O}_{WP}$ has no significant change during each segment, but both $\mathbf{O}_{w1}$ and $\mathbf{O}_{w2}$ clearly vary around $\mathbf{O}_{WP}$. During the whole interval in Figure 5, the standard deviations of the X, Y, and Z components of $\mathbf{O}_{WP} - \mathbf{O}_{w1}$ ($\mathbf{O}_{WP} - \mathbf{O}_{w2}$) are 3.06, 2.44, and 2.89 (2.26, 1.29, and 1.99) nT, respectively. This suggests that more subinterval events can make the calculation error of the Wang method II smaller. The averages of the X, Y, and Z components of $\mathbf{O}_{WP} - \mathbf{O}_{w1}$ ($\mathbf{O}_{WP} - \mathbf{O}_{w2}$) are −0.05, 0.55, and −0.87 (−0.23, 0.24, and 0.07) nT, respectively. The zero offset determined by this method has a 27-day quasi-periodic variation (Wang, 2022c), but the Wang-Pan method I has no such a quasi-periodic variation (Wang & Pan, 2021a). This might explain why the standard deviation of $\mathbf{O}_{WP} - \mathbf{O}_{w1}$ (or $\mathbf{O}_{WP} - \mathbf{O}_{w2}$) is somewhat large but its average is close to 0.

In order to reduce the effect of the 27-day cycle change of the zero offset determined by the Wang method II, the estimated zero offset should be smoothed with a 27-day boxcar filter (Wang, 2022c). Before performing smoothing, the estimated zero offset can be interpolated into the time series of the magnetic field $\mathbf{B}_2$. Figure 6 shows

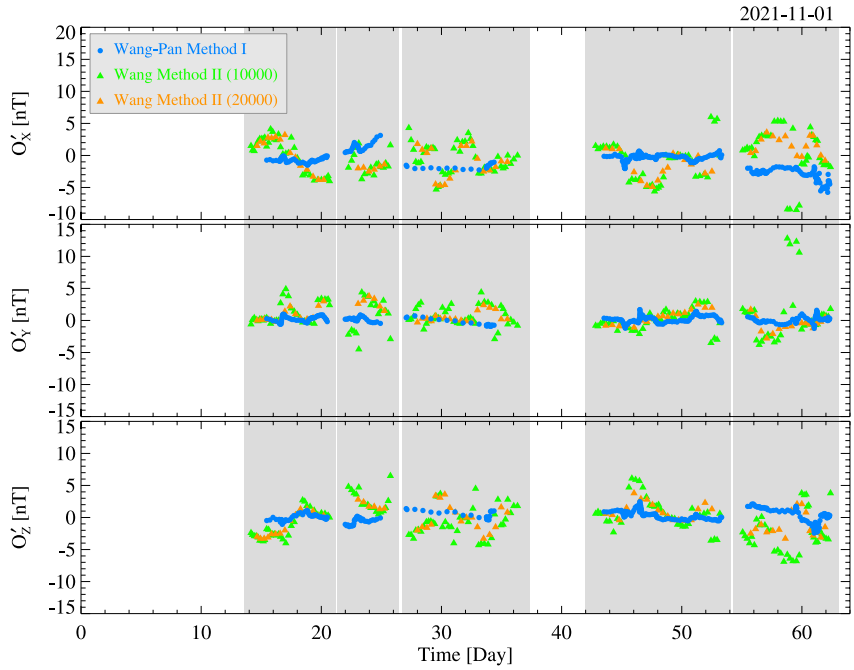

Figure 5. Three components of the zero offsets determined by the Wang method II using 10,000 (green) and 20,000 (orange) adjacent subinterval events and the Wang-Pan method I using 10 adjacent potential Alfvénic fluctuation events (blue) during the period from 13 November 2021 to 3 January 2022. Each gray region denotes a data segment without gaps.

the averages of $\mathbf{O}_{WP}$, $\mathbf{O}_{W1}$, and $\mathbf{O}_{W2}$ during each segment instead of smoothing with a 27-day boxcar filter, since the maximum duration of the data segment we used is ∼14 days. The differences of the X or Z component of the average $\mathbf{O}_{WP}$ minus the average $\mathbf{O}_{W1}$ changes sign from one segment to the next. The second segment as shown in the gray shaded region in Figure 6 has a duration of ∼5 days, and the average $\mathbf{O}_{W1}$ deviates more from the average

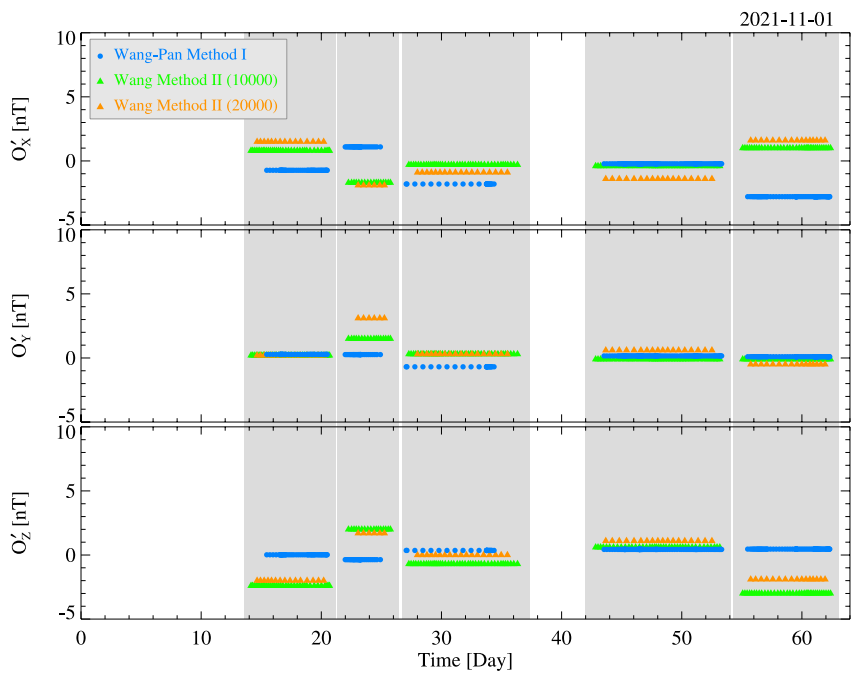

Figure 6. Three components of the average zero offsets determined by the Wang method II using 10,000 (green) and 20,000 (orange) adjacent events and the Wang-Pan method I using 10 adjacent potential Alfvénic fluctuation events (blue) during each segment. Each gray region denotes a data segment without gaps.

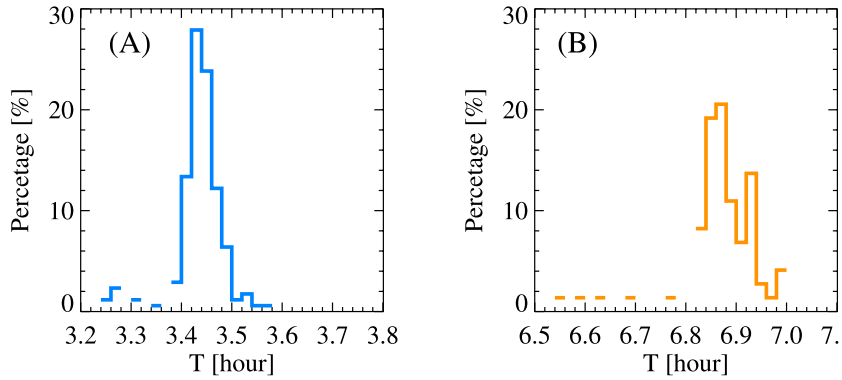

Figure 7. Histograms of the amount of the data used to determine each zero offset by the Wang method II when using 10,000 (a) and 20,000 (b) adjacent events.

$\mathbf{O}_{WP}$ than that in the fourth segment. This is in agreement with the 27-day cycle variation of the zero offset determined by Wang method II (Wang, 2022c). It suggests that the segment with a duration of <27 days might have a larger calculation error of the zero offset if its duration is shorter.

When we select 10,000 or 20,000 adjacent subinterval events to determine the zero offset by the Wang method II, the data at a certain time might belong to several different subintervals. To obtain the amount of the data (T_d) we used to calculate each zero offset, the time of the data belonging to several subintervals is counted only once. Figure 7a shows the distribution of T_d when using 10,000 adjacent subinterval events. T_d is mainly in the range of 3.2–3.6 hr. Figure 7b shows that T_d is mainly in the range of 6.5–7 hr when using 20,000 adjacent subinterval events. Therefore, several hours of the data in the Martian magnetosheath is able to make the Wang method II perform the calculation of the zero offset.

4. Discussion and Summary

The Wang method II can use any IMF fluctuations to perform the in-flight calibration, and its accuracy of the estimated zero offset is associated with the amount of the used IMF data (Wang, 2022b). For example, this method has a 78.7% (95.5%) probability to achieve an accuracy of 0.3 nT when using 8–14 (10–21) hours of the IMF data measured by the Magnetospheric Multiscale (MMS) mission (Burch et al., 2016). Wang (2022c) tested the performance of the Wang method II in the Martian magnetosheath using the calibrated magnetic field data measured by the MAVEN spacecraft. The test results showed that the accuracy of this method is affected by the number of the used subintervals, position of the spacecraft and the eigenvalues of the MVA (Wang, 2022c). The accuracy tends to be higher when the spacecraft moves away from the Mars-Sun line (Wang, 2022c). The apoareon altitude of the MAVEN spacecraft is ~6,220 km (Jakosky et al., 2015), much smaller than that of the Tianwen-1 orbiter. Thus, the Wang method II is expected to have a better performance in the Martian magnetosheath for the Tianwen-1 orbiter than that for the MAVEN spacecraft according to the findings of Wang (2022c).

In the solar wind, the Wang method II can achieve a high accuracy of the zero offset possibly because of each component of the IMF having a median of ~0 over a long enough period (Wang, 2022b). Wang (2022c) tested the Wang method II in the Martian magnetosheath using the MAVEN data, and found that the estimated zero offset has a time-varying calculation error with an amplitude of 1–4 nT and a period of ~27 days. At a certain position in the Martian magnetosheath, the distribution of each component of the magnetic field over several days can be affected by the upstream IMF (see Wang, 2022c). The median of this distribution is found to be varied around 0 with a period of ~27 days (see Wang, 2022c). This might be one reason why the zero offset determined by the Wang method II has calculation errors with a period of ~27 days, since the nonzero of the median of the magnetic field distribution could introduce calculation errors to the Wang method II (Wang, 2022c). We speculate that the 27-day periodicity of the median of the magnetic field in the Martian magnetosheath might be associated with the 27-day periodicity of the IMF (Castillo et al., 2021).

In order to obtain an accurate zero offset, $\mathbf{O}_{W1}$ (or $\mathbf{O}_{W2}$) should be smoothed with a temporal window of 27 days. Before smoothing, $\mathbf{O}_{W1}$ (or $\mathbf{O}_{W2}$) can be interpolated into a continuous time series, which start and end times are

the same with the corresponding segment. In our test, the durations of the segments we used are ∼5–14 days, much shorter than 27 days. And the difference between the average $\mathbf{O}_{Wp}$ and the average $\mathbf{O}_{W1}$ can be up to 3 nT during some segments (see Figure 6). Figure 6 also shows that such a difference tends to be smaller if the data segment's duration is longer. For example, the difference between the average $\mathbf{O}_{Wp}$ and the average $\mathbf{O}_{W1}$ is < 1 nT during the fourth data segment (see Figure 6). Therefore, one can expect that the Wang method II is able to achieve a good calibration if the data segment's duration is longer than 27 days.

In summary, we test the performance of the Wang method II in the Martian magnetosheath using the uncalibrated magnetic field data measured by the Tianwen-1 orbiter from 13 November 2021 to 3 January 2022. Compared to the zero offsets $\mathbf{O}_{wp}$ determined by the Wang-Pan method I using the potential Alfvénic fluctuation events in the solar wind, the zero offsets $\mathbf{O}_{w}$ determined by the Wang method II vary around $\mathbf{O}_{wp}$. When the data segment has a duration of <27 days, $\mathbf{O}_{w}$ tends to have a larger error if the duration is shorter. Although the Wang method II might have a large calculation error of the zero offset in a single calculation, the error will decrease after smoothing the zero offset with a temporal window of 27 days. Our results suggest that the Wang method II is suitable for determine the zero offset of the MOMAG in the Marian magnetosheath if the duration of the data segment is long enough, such as 14 days.

Data Availability Statement

The Tianwen-1/MOMAG data are publicly available at CNSA Data Release System (https://space.ustc.edu.cn/dreams/tw1_momag/). The data used in this paper can be downloaded from the official website of the MOMAG team (http://space.ustc.edu.cn/dreams/tw1_momag/).

Acknowledgments
This work was supported by NSFC (42130204, 42241155, 41974205, 42241133, 42188101), Guangdong Basic and Applied Basic Research Foundation (2022A1515011698, 2023A1515030132, 2022A1515010257), Shenzhen Science and Technology Research Program (JCYJ20210324121412034, JCYJ20210324121403009), the Fundamental Research Funds for the Central Universities (HIT.OCEF.2022041), Shenzhen Key Laboratory Launching Project (ZDSYS20210702140800001), Strategic Priority Program of the Chinese Academy of Sciences (XDB41000000), the Macau foundation, the pre-research Project on Civil Aerospace Technologies (D020103) funded by CNSA, and CAS Center for Excellence in Comparative Planetology. Y.W. is particularly grateful for the support of the Tencent Foundation. We acknowledge the Tianwen-1 team for the magnetic field data.

References

Belcher, J. W. (1973). Variation of Davis-Smith method for in-flight determination of spacecraft magnetic-fields. *Journal of Geophysical Research*, *78*(28), 6480–6490. https://doi.org/10.1029/JA078i028p06480

Bertucci, C., Duru, F., Edberg, N., Fraenz, M., Martinecz, C., Szego, K., & Vaisberg, O. (2011). The induced magnetospheres of Mars, Venus, and Titan. *Space Science Reviews*, *162*(1–4), 113–171. https://doi.org/10.1007/s11214-011-9845-1

Burch, J. L., Moore, T. E., Torbert, R. B., & Giles, B. L. (2016). Magnetospheric multiscale overview and science objectives. *Space Science Reviews*, *199*(1–4), 5–21. https://doi.org/10.1007/s11214-015-0164-9

Castillo, Y., Pais, M. A., Fernandes, J., Ribeiro, P., Morozova, A. L., & Pinheiro, F. J. G. (2021). Relating 27-day averages of solar, interplanetary medium parameters, and geomagnetic activity proxies in solar cycle 24. *Solar Physics*, *296*(7), 115. https://doi.org/10.1007/s11207-021-01856-8

Chai, L. H., Wan, W. X., Wei, Y., Zhang, T. L., Exner, W., Fraenz, M., et al. (2019). The induced global looping magnetic field on Mars. *The Astrophysical Journal Letters*, *871*(2), L27. https://doi.org/10.3847/2041-8213/aaff6e

Cheng, S. N., Wang, G. Q., Pan, Z. H., Meng, L. F., Yi, Z., & Zhang, T. L. (2022). An optimal method for in-flight calibration of the fluxgate magnetometer when the total magnetic field of Alfven waves has a drift trend. *Chinese Journal of Geophysics*, *65*(5), 1558–1570. https://doi.org/10.6038/cjg2022P0362

Connerney, J. E. P., Acuna, M. H., Ness, N. F., Kletetschka, G., Mitchell, D. L., Lin, R. P., & Reme, H. (2005). Tectonic implications of Mars crustal magnetism. *Proceedings of the National Academy of Sciences of the United States of America*, *102*(42), 14970–14975. https://doi.org/10.1073/pnas.0507469102

Connerney, J. E. P., Espley, J., Lawton, P., Murphy, S., Odom, J., Oliversen, R., & Sheppard, D. (2015). The MAVEN magnetic field investigation. *Space Science Reviews*, *195*(1–4), 257–291. https://doi.org/10.1007/s11214-015-0169-4

Davis, L., & Smith, E. J. (1968). The in-flight determination of spacecraft magnetic field zeros. *EOS Transaction American Geophysical Union*, *49*, 257.

DiBraccio, G. A., Espley, J. R., Gruesbeck, J. R., Connerney, J. E. P., Brain, D. A., Halekas, J. S., et al. (2015). Magnetotail dynamics at mars: Initial MAVEN observations. *Geophysical Research Letters*, *42*(21), 8828–8837. https://doi.org/10.1002/2015gl065248

Dubinin, E., Modolo, R., Fraenz, M., Päetzold, M., Woch, J., Chai, L., et al. (2019). The induced magnetosphere of Mars: Asymmetrical topology of the magnetic field lines. *Geophysical Research Letters*, *46*(22), 12722–12730. https://doi.org/10.1029/2019gl084387

Edberg, N. J. T., Brain, D. A., Lester, M., Cowley, S. W. H., Modolo, R., Franz, M., & Barabash, S. (2009). Plasma boundary variability at mars as observed by mars global surveyor and mars express. *Annales Geophysicae*, *27*(9), 3537–3550. https://doi.org/10.5194/angeo-27-3537-2009

Edberg, N. J. T., Lester, M., Cowley, S. W. H., & Eriksson, A. I. (2008). Statistical analysis of the location of the Martian magnetic pileup boundary and bow shock and the influence of crustal magnetic fields. *Journal of Geophysical Research*, *113*(A8), A08206. https://doi.org/10.1029/2008ja013096

Fang, X. H., Ma, Y. J., Luhmann, J., Dong, Y. X., Brain, D., Hurley, D., et al. (2018). The morphology of the solar wind magnetic field draping on the dayside of Mars and its variability. *Geophysical Research Letters*, *45*(8), 3356–3365. https://doi.org/10.1002/2018gl077230

Hedgecock, P. C. (1975). A correlation technique for magnetometer zero level determination. *Space Science Instrumentation*, *1*(1), 83–90.

Hu, X. W., Wang, G. Q., Pan, Z. H., & Pan, Z. (2022a). Automatic calculation of the magnetometer zero offset using the interplanetary magnetic field based on the Wang–Pan method. *Earth and Planetary Physics*, *6*(1), 1–60. https://doi.org/10.26464/epp2022017

Hu, X. W., Wang, G. Q., Pan, Z. H., & Zhang, T. L. (2022). Application of the Wang–Pan method based on mirror mode structures on the in-flight calibration of magnetometers. *Chinese Journal of Geophysics*, *65*(6), 1940–1950. https://doi.org/10.6038/cjg2022P0640

Jakosky, B. M., Lin, R. P., Grebowsky, J. M., Luhmann, J. G., Mitchell, D. F., Beutelschies, G., et al. (2015). The mars atmosphere and volatile evolution (MAVEN) mission. *Space Science Reviews*, *195*(1–4), 3–48. https://doi.org/10.1007/s11214-015-0139-x

Leinweber, H. K., Russell, C. T., Torkar, K., Zhang, T. L., & Angelopoulos, V. (2008). An advanced approach to finding magnetometer zero levels in the interplanetary magnetic field. *Measurement Science and Technology*, *19*(5), 055104. https://doi.org/10.1088/0957-0233/19/5/055104

Li, C. L., Zhang, R. Q., Yu, D. Y., Dong, G. L., Liu, J. J., Geng, Y., et al. (2021). China's Mars exploration mission and science investigation. *Space Science Reviews*, *217*(4), 57. https://doi.org/10.1007/s11214-021-00832-9

Liu, D., Rong, Z., Gao, J., He, J., Klinger, L., Dunlop, M. W., et al. (2021). Statistical properties of solar wind upstream of mars: MAVEN observations. *The Astrophysical Journal*, *911*(2), 113. https://doi.org/10.3847/1538-4357/abed50

Liu, K., Hao, X. J., Li, Y. R., Zhang, T. L., Pan, Z. H., Chen, M. M., et al. (2020). Mars orbiter magnetometer of China's first Mars mission Tianwen-1. *Earth and Planetary Physics*, *4*(4), 384–389. https://doi.org/10.26464/epp2020058

Meng, L. F., Pan, Z. H., Yi, Z., Wang, G. Q., & Zhang, T. L. (2018). Error properties of the fluxgate magnetometer offset based on Davis-Smith method. *Chinese Journal of Geophysics*, *61*(9), 3545–3551. https://doi.org/10.6038/cjg2018L0264

Meng, L. F., & Wang, G. Q. (2023). A new method for in-flight calibration of spaceborne fluxgate magnetometers based on Alfvénic nature of the interplanetary magnetic field. *Chinese Journal of Geophysics*, *66*(5). (in Chinese). https://doi.org/10.6038/cjg2022Q0246

Ness, N. F., Behannon, K. W., Lepping, R. P., & Schatten, K. H. (1971). Use of two magnetometers for magnetic field measurements on a spacecraft. *Journal of Geophysical Research*, *76*(16), 3564–3573. https://doi.org/10.1029/JA076i016p03564

Pan, Z. H., Wang, G. Q., Meng, L. F., Yi, Z., & Zhang, T. L. (2019). Influence of Alfvénic characteristics on calibration of satellite magnetometer. *Chinese Journal of Geophysics*, *62*(4), 1193–1198. https://doi.org/10.6038/cjg2019M0513

Plaschke, F., Goetz, C., Volwerk, M., Richter, I., Fruhauff, D., Narita, Y., et al. (2017). Fluxgate magnetometer offset vector determination by the 3D mirror mode method. *Monthly Notices of the Royal Astronomical Society*, *469*(Suppl_2), S675–S684. https://doi.org/10.1093/mnras/stx2532

Plaschke, F., & Narita, Y. (2016). On determining fluxgate magnetometer spin axis offsets from mirror mode observations. *Annales Geophysicae*, *34*(9), 759–766. https://doi.org/10.5194/angeo-34-759-2016

Pope, S. A., Zhang, T. L., Balikhin, M. A., Delva, M., Hvizdos, L., Kudela, K., & Dimmock, A. P. (2011). Exploring planetary magnetic environments using magnetically unclean spacecraft: A systems approach to VEX MAG data analysis. *Annales Geophysicae*, *29*(4), 639–647. https://doi.org/10.5194/angeo-29-639-2011

Russell, C. T., Anderson, B. J., Baumjohann, W., Bromund, K. R., Dearborn, D., Fischer, D., et al. (2016). The magnetospheric multiscale magnetometers. *Space Science Reviews*, *199*(1–4), 189–256. https://doi.org/10.1007/s11214-014-0057-3

Sonnerup, B. U. Ö., & Scheible, M. (1998). Minimum and maximum variance analysis. *ISSI Scientific Report Series*, *1*, 185–220.

Tsurutani, B. T., Lakhina, G. S., Verkhoglyadova, O. P., Echer, E., Guarnieri, F. L., Narita, Y., & Constantinescu, D. O. (2011). Magnetosheath and heliosheath mirror mode structures, interplanetary magnetic decreases, and linear magnetic decreases: Differences and distinguishing features. *Journal of Geophysical Research*, *116*(A2), A02103. https://doi.org/10.1029/2010ja015913

Volwerk, M., Schmid, D., Tsurutani, B. T., Delva, M., Plaschke, F., Narita, Y., et al. (2016). Mirror mode waves in Venus's magnetosheath: Solar minimum vs. solar maximum. *Annales Geophysicae*, *34*(11), 1099–1108. https://doi.org/10.5194/angeo-34-1099-2016

Volwerk, M., Zhang, T. L., Delva, M., Vörös, Z., Baumjohann, W., & Glassmeier, K. H. (2008). First identification of mirror mode waves in Venus' magnetosheath? *Geophysical Research Letters*, *35*(12), L12204. https://doi.org/10.1029/2008gl033621

Wang, G. Q. (2022a). High-precision calibration of the fluxgate magnetometer offset vector in the terrestrial magnetosheath. *The Astrophysical Journal*, *929*(1), 87. https://doi.org/10.3847/1538-4357/ac5907

Wang, G. Q. (2022b). A new method of fluxgate magnetometer offset vector determination in the solar wind using any magnetic field variations. *The Astrophysical Journal*, *935*(2), 147. https://doi.org/10.3847/1538-4357/ac822c

Wang, G. Q. (2022c). In-flight calibration of the spaceborne fluxgate magnetometer in the Martian magnetosheath. *Earth and Planetary Physics*, *6*(6), 1–600. https://doi.org/10.26464/epp2022047

Wang, G. Q., & Pan, Z. H. (2021a). A new method to calculate the fluxgate magnetometer offset in the interplanetary magnetic field: 1. Using Alfvén waves. *Journal of Geophysical Research: Space Physics*, *126*(4), e2020JA028893. https://doi.org/10.1029/2020ja028893

Wang, G. Q., & Pan, Z. H. (2021b). A new method to calculate the fluxgate magnetometer offset in the interplanetary magnetic field: 2. Using mirror mode structures. *Journal of Geophysical Research: Space Physics*, *126*(9), e2021JA029781. https://doi.org/10.1029/2021ja029781

Wang, G. Q., & Pan, Z. H. (2022). Fluxgate magnetometer offset vector determination using current sheets in the solar wind. *The Astrophysical Journal*, *926*(1), 12. https://doi.org/10.3847/1538-4357/ac3d8f

Wang, G. Q., Volwerk, M., Du, A. M., Xiao, S. D., Wu, M. Y., Chen, Y. Q., & Zhang, T. L. (2021). Statistical study of small-scale magnetic holes in the upstream regime of the Martian bow shock. *The Astrophysical Journal*, *921*(2), 153. https://doi.org/10.3847/1538-4357/ac1c07

Wang, Y. M., Zhang, T. L., Wang, G. Q., Xiao, S. D., Zou, Z. X., Cheng, L., et al. (2023). The Mars orbiter magnetometer of Tianwen-1: In-flight performance and first science results. *Earth and Planetary Physics*, *7*(2), 1–228. https://doi.org/10.26464/epp2023028

Wu, M. Y., Chen, Y. J., Du, A. M., Wang, G. Q., Xiao, S. D., Peng, E., et al. (2021). Statistical properties of small-scale linear magnetic holes in the Martian magnetosheath. *The Astrophysical Journal*, *916*(2), 104. https://doi.org/10.3847/1538-4357/ac090b

Xu, S. S., Mitchell, D. L., McFadden, J. P., Collinson, G., Harada, Y., Lillis, R., et al. (2018). Field-aligned potentials at mars from MAVEN observations. *Geophysical Research Letters*, *45*(19), 10119–10127. https://doi.org/10.1029/2018gl080136

Yang, Y. Y., Zhou, B., Hulot, G., Olsen, N., Wu, Y. Y., Xiong, C., et al. (2021). CSES high precision magnetometer data products and example study of an intense geomagnetic storm. *Journal of Geophysical Research: Space Physics*, *126*(4), e2020JA028026. https://doi.org/10.1029/2020ja028026

Zhou, B., Cheng, B. J., Gou, X. C., Li, L., Zhang, Y. T., Wang, J. D., et al. (2019). First in-orbit results of the vector magnetic field measurement of the High Precision Magnetometer onboard the China Seismo-Electromagnetic Satellite. *Earth Planets and Space*, *71*(1), 119. https://doi.org/10.1186/s40623-019-1098-3

Zou, Y. L., Zhu, Y., Bai, Y. F., Wang, L. G., Jia, Y. Z., Shen, W. H., et al. (2021). Scientific objectives and payloads of Tianwen-1, China's first Mars exploration mission. *Advances in Space Research*, *67*(2), 812–823. https://doi.org/10.1016/j.asr.2020.11.005

Zou, Z. X., Wang, Y. M., Zhang, T. L., Wang, G. Q., Xiao, S. D., Pan, Z. H., et al. (2023). In-flight calibration of the magnetometer on the mars orbiter of Tianwen-1. *Science China Technological Sciences*, *66*(8), 2396–2405. https://doi.org/10.1007/s11431-023-2401-2